

Ab initio study of the photoabsorption of ${}^4\text{He}$

W. Horiuchi,¹ Y. Suzuki,^{2,1} and K. Arai³

¹*RIKEN Nishina Center, Wako 351-0198, Japan*

²*Department of Physics, Niigata University, Niigata 950-2181, Japan*

³*Division of General Education, Nagaoka National College of Technology, Nagaoka 940-8532, Japan*

There are some discrepancies in the low energy data on the photoabsorption cross section of ${}^4\text{He}$. We calculate the cross section with realistic nuclear forces and explicitly correlated Gaussian functions. Final state interactions and two- and three-body decay channels are taken into account. The cross section is evaluated in two methods: With the complex scaling method the total absorption cross section is obtained up to the rest energy of a pion, and with the microscopic R -matrix method both cross sections ${}^4\text{He}(\gamma, p){}^3\text{H}$ and ${}^4\text{He}(\gamma, n){}^3\text{He}$ are calculated below 40 MeV. Both methods give virtually the same result. The cross section rises sharply from the ${}^3\text{H}+p$ threshold, reaching a giant resonance peak at 26–27 MeV. Our calculation reproduces almost all the data above 30 MeV. We stress the importance of ${}^3\text{H}+p$ and ${}^3\text{He}+n$ cluster configurations on the cross section as well as the effect of the one-pion exchange potential on the photonuclear sum rule.

PACS numbers: 25.20.Dc, 25.40.Lw, 27.10.+h, 21.60.De

I. INTRODUCTION

Nuclear strength or response functions for electroweak interactions provide us with important information on the resonant and continuum structure of the nuclear system as well as the detailed property of the underlying interactions. In this paper we focus on the photoabsorption of ${}^4\text{He}$. The experimental study of (γ, p) and (γ, n) reactions on ${}^4\text{He}$ has a long history over the last half century. See Refs. [1–3] and references therein. Unfortunately the experimental data presented so far are in serious disagreement, and thus a measurement of the photoabsorption cross section is still actively performed with different techniques in order to resolve this enigma [4, 5].

Calculations of the cross section on ${}^4\text{He}$ have been performed in several methods focusing on e.g., the peak position of the giant electric dipole ($E1$) resonance, charge symmetry breaking effects, and $E1$ sum rules [6–8]. The photoabsorption cross section has extensively been calculated in the Lorentz integral transform (LIT) method [9], among others, which does not require calculating continuum wave functions. In the LIT the cross section is obtained by inverting the integral transform of the strength function, which is calculable using square-integrable (\mathcal{L}^2) functions. The calculations were done with Malfliet-Tjon central force [3], the realistic Argonne $v18$ potential [10, 11], and an interaction based on chiral effective field theory [12].

In the calculations with the realistic interactions some singular nature of them, especially the short-range repulsion, has been appropriately replaced with the effective one that adapts to the model space of the respective approaches, that is, the hyperspherical harmonics method [10, 11] and the no-core shell model [12]. All of these calculations show the cross section that disagrees with the data [1] especially in the low excitation energy near the ${}^3\text{H}+p$ threshold. The resonance peak obtained theoretically appears at about 27 MeV consistently with the experiments [2, 4, 5], but in a marked difference from

that of Ref. [1].

We have recently reported that all the observed levels of ${}^4\text{He}$ below 26 MeV are well reproduced in a four-body calculation using bare realistic nuclear interactions [13, 14]. It is found that using the realistic interaction is vital to reproduce the ${}^4\text{He}$ spectrum as well as the well-developed $3N+N$ (${}^3\text{H}+p$ and ${}^3\text{He}+n$) cluster states with positive and negative parities. In this calculation the wave functions of the states are approximated in a combination of explicitly correlated Gaussians [15, 16] reinforced with a global vector representation for the angular motion [17, 18]. Furthermore this approach has very recently been applied to successfully describe four-nucleon scattering and reactions [19, 20] with the aid of a microscopic R -matrix method (MRM) [21]. It is found that the tensor force plays a crucial role in accounting for the astrophysical S factors of the radiative capture reaction ${}^2\text{H}(d, \gamma){}^4\text{He}$ as well as the nucleon transfer reactions, ${}^2\text{H}(d, p){}^3\text{H}$ and ${}^2\text{H}(d, n){}^3\text{He}$ [19].

The aim of this paper is to examine the issue of the photoabsorption cross section of ${}^4\text{He}$. Because four-body bound state problems with realistic nucleon-nucleon (NN) interactions can be accurately solved with the correlated Gaussians, it is interesting to apply that approach to a calculation of the photoabsorption cross section. For this purpose we have to convert the continuum problem to such a bound-state like problem that can be treated in the \mathcal{L}^2 basis functions. Differently from the previous theoretical calculations [3, 10–12], we employ a complex scaling method (CSM) [22–24] for avoiding a construction of the continuum wave functions. One of the advantages of the CSM is that the cross section can be directly obtained without recourse to a sophisticated inversion technique as used in the LIT or an artificial energy averaging procedure. We will pay special attention to the following points:

1. To use a realistic interaction as it is
2. To include couplings with final decay channels explicitly

3. To perform calculations in both MRM and CSM as a cross-check.

Here point (1) indicates that the interaction is not changed to an effective force by some transformation. This looks sound and appealing because the cross section may depend on the D -state probability of ${}^4\text{He}$ [7] and hence the effect of the tensor force on the cross section could be seen directly. In point (2) we make use of the flexibility of the correlated Gaussians to include such important configurations that have ${}^3\text{H}+p$, ${}^3\text{He}+n$, and $d+p+n$ partitions. Thanks to this treatment the effects of final-state interactions are expected to be fully taken into account. Point (3) is probably most significant in our approach. We mean by this point that the photoabsorption cross section is calculated in two independent methods. In the MRM we calculate the cross sections for the radiative capture reactions, ${}^3\text{H}(p, \gamma){}^4\text{He}$ and ${}^3\text{He}(n, \gamma){}^4\text{He}$, and these cross sections are converted to the photoabsorption cross section using a formula due to the detailed balance. In the CSM we make use of the fact that the final continuum states of ${}^4\text{He}$, if rotated on the complex coordinate plane, can be expanded in the \mathcal{L}^2 functions. Consistency of the two results, if attained, serves strong evidence for that the obtained cross section is reliable. We hope to shed light on resolving the controversy from our theoretical input.

In Sec. II we present our theoretical prescriptions to calculate the photoabsorption cross section. The two approaches, the CSM and the MRM, are explained in this section with emphasis on the method of how discretized states are employed for the continuum problem. We give the basic inputs of our calculation in Sec. III. The detail of our correlated basis functions is given in Sec. III B, and various configurations needed to take into account the final state interactions as well as two- and three-body decay channels are explained in Sec. III D. We show results on the photoabsorption cross section in Sec. IV. The $E1$ strength function and the transition densities calculated from the continuum discretized states are presented in Sec. IV A. A comparison of CSM and MRM cross sections is made in Sec. IV B. The photonuclear sum rules are examined in Sec. IV C. The calculated photoabsorption cross sections are compared to experiment in Sec. IV D. Finally we draw conclusions of this work in Sec. V.

II. FORMULATION OF PHOTOABSORPTION CROSS SECTION CALCULATION

A. Basic formula

The photoabsorption takes place mainly through the $E1$ transition, which can be treated by the perturbation theory. The wavelength of the photon energy E_γ (MeV) is about $1240/E_\gamma$ (fm), so that it is long enough compared to the radius of ${}^4\text{He}$ even when E_γ is close to the rest energy of a pion. The photoabsorption cross section

$\sigma_\gamma(E_\gamma)$ can be calculated by the formula [25]

$$\sigma_\gamma(E_\gamma) = \frac{4\pi^2}{\hbar c} E_\gamma \frac{1}{3} S(E_\gamma), \quad (1)$$

where $S(E)$ is the strength function for the $E1$ transition

$$S(E) = \mathcal{S}_{\mu f} |\langle \Psi_f | \mathcal{M}_{1\mu} | \Psi_0 \rangle|^2 \delta(E_f - E_0 - E). \quad (2)$$

The symbol $\mathcal{M}_{1\mu}$ denotes the $E1$ operator, and Ψ_0 and Ψ_f are the wave functions of the ground state with energy E_0 and the final state with the excitation energy E_f of ${}^4\text{He}$, respectively. The recoil energy of ${}^4\text{He}$ is ignored, so that E_γ is equal to the nuclear excitation energy E . The symbol $\mathcal{S}_{\mu f}$ indicates a summation over μ and all possible final states f . The final state of ${}^4\text{He}$ is actually a continuum state lying above the ${}^3\text{H}+p$ threshold, and it is normalized according to $\langle \Psi_{f'} | \Psi_f \rangle = \delta(E_{f'} - E_f)$. The sum or integral for the final states in $\mathcal{S}_{\mu f}$ can be taken using the closure relation, leading to a well-known expression for the strength function

$$S(E) = -\frac{1}{\pi} \text{Im} \sum_{\mu} \langle \Psi_0 | \mathcal{M}_{1\mu}^\dagger \frac{1}{E - H + i\epsilon} \mathcal{M}_{1\mu} | \Psi_0 \rangle, \quad (3)$$

where a positive infinitesimal ϵ ensures the outgoing wave after the excitation of ${}^4\text{He}$. A method of calculation of $S(E)$ in the CSM is presented in Sec. II B.

A partial photoabsorption cross section $\sigma_\gamma^{\text{AB}}(E_\gamma)$ for the two-body final state comprising nuclei, A and B, can be calculated in another way. With use of the detailed balance the cross section is related to that of its inverse process, the radiative capture cross section $\sigma_{\text{cap}}^{\text{AB}}(E_{\text{in}})$ [26], induced by the $E1$ transition, at the incident energy $E_{\text{in}} = E_\gamma - E_{\text{th}}$,

$$\sigma_\gamma^{\text{AB}}(E_\gamma) = \frac{k^2(2J_A + 1)(2J_B + 1)}{2k_\gamma^2(2J_0 + 1)} \sigma_{\text{cap}}^{\text{AB}}(E_{\text{in}}), \quad (4)$$

where E_{th} is the A+B threshold energy. Here J_A and J_B are the angular momenta of the nuclei, A and B, and $J_0 (= 0)$ is the angular momentum of the ground state of ${}^4\text{He}$. The wave number k is $\sqrt{2\mu_{AB}E_{\text{in}}/\hbar^2}$ where μ_{AB} is the reduced mass of the two nuclei and k_γ is the photon wave number $E_\gamma/\hbar c$. The photoabsorption cross section $\sigma_\gamma(E_\gamma)$ is equal to a sum of $\sigma_\gamma^{{}^3\text{H}p}(E_\gamma)$ and $\sigma_\gamma^{{}^3\text{He}n}(E_\gamma)$ provided that three- and four-body breakup contributions are negligible. A calculation of the radiative capture cross section will be performed in the MRM as explained in Sec. II C.

The fact that we have two independent methods of calculating $\sigma_\gamma(E_\gamma)$ is quite important to assess their validity.

B. Complex scaling method

The quantity $S(E)$ of Eq. (3) is evaluated using the CSM, which makes a continuum state that has an outgoing wave in the asymptotic region damp at large distances, thus enabling us to avoid an explicit construction

of the continuum state. In the CSM the single particle coordinate \mathbf{r}_j and momentum \mathbf{p}_j are subject to a rotation by an angle θ :

$$U(\theta) : \quad \mathbf{r}_j \rightarrow \mathbf{r}_j e^{i\theta}, \quad \mathbf{p}_j \rightarrow \mathbf{p}_j e^{-i\theta}. \quad (5)$$

Applying this transformation in Eq. (3) leads to

$$S(E) = -\frac{1}{\pi} \text{Im} \sum_{\mu} \langle \Psi_0 | \mathcal{M}_{1\mu}^{\dagger} U^{-1}(\theta) R(\theta) U(\theta) \mathcal{M}_{1\mu} | \Psi_0 \rangle, \quad (6)$$

where $R(\theta)$ is the complex scaled resolvent

$$R(\theta) = \frac{1}{E - H(\theta) + i\epsilon} \quad (7)$$

with

$$H(\theta) = U(\theta) H U^{-1}(\theta). \quad (8)$$

A key point in the CSM is that within a suitable range of positive θ the eigenvalue problem

$$H(\theta) \Psi_{\lambda}^{JM\pi}(\theta) = E_{\lambda}(\theta) \Psi_{\lambda}^{JM\pi}(\theta) \quad (9)$$

can be solved in a set of \mathcal{L}^2 basis functions $\Phi_i(\mathbf{x})$

$$\Psi_{\lambda}^{JM\pi}(\theta) = \sum_i C_i^{\lambda}(\theta) \Phi_i(\mathbf{x}). \quad (10)$$

We are interested in $\Psi_{\lambda}^{JM\pi}(\theta)$ with $J^{\pi} = 1^{-}$. With the solution of Eq. (9), an expression for $S(E)$ reads [27, 28]

$$S(E) = -\frac{1}{\pi} \sum_{\mu\lambda} \text{Im} \frac{\widetilde{\mathcal{D}}_{\mu}^{\lambda}(\theta) \mathcal{D}_{\mu}^{\lambda}(\theta)}{E - E_{\lambda}(\theta) + i\epsilon}, \quad (11)$$

where

$$\begin{aligned} \mathcal{D}_{\mu}^{\lambda}(\theta) &= \langle (\Psi_{\lambda}^{JM\pi}(\theta))^* | \mathcal{M}_{1\mu}(\theta) | U(\theta) \Psi_0 \rangle, \\ \widetilde{\mathcal{D}}_{\mu}^{\lambda}(\theta) &= \langle (U(\theta) \Psi_0)^* | \widetilde{\mathcal{M}}_{1\mu}(\theta) | \Psi_{\lambda}^{JM\pi}(\theta) \rangle, \end{aligned} \quad (12)$$

with

$$\begin{aligned} \mathcal{M}_{1\mu}(\theta) &= U(\theta) \mathcal{M}_{1\mu} U^{-1}(\theta) = \mathcal{M}_{1\mu} e^{i\theta}, \\ \widetilde{\mathcal{M}}_{1\mu}(\theta) &= U(\theta) \mathcal{M}_{1\mu}^{\dagger} U^{-1}(\theta) = \mathcal{M}_{1\mu}^{\dagger} e^{i\theta}. \end{aligned} \quad (13)$$

Note that the energy of the bound state of H in principle remains the same against the scaling angle θ . Also $U(\theta) \Psi_0$ is to be understood as a solution of Eq. (9) for $J^{\pi} = 0^{+}$ corresponding to the ground-state energy [28]. This stability condition will be met when the basis functions are chosen sufficiently.

In such a case where sharp resonances exist, the angle θ has to be rotated to cover their resonance poles on the complex energy plane [23, 24]. A choice of θ is made by examining the stability of $S(E)$ with respect to the angle. One of the advantages of the CSM is that one needs no artificial energy smoothing procedure but obtains the continuous cross section naturally.

C. Microscopic R -matrix method

The calculation of $\sigma_{\text{cap}}^{\text{AB}}(E_{\text{in}})$ involves the matrix element of $\mathcal{M}_{1\mu}$ between the scattering state initiated through the A+B entrance channel and the final state, i.e., the ground state of ${}^4\text{He}$. See, e.g., Ref. [29]. The scattering problem is solved in the MRM. As is discussed in detail for the four-nucleon scattering [20, 30], an accurate solution for the scattering problem with realistic NN potentials in general requires a full account of couplings of various channels. In the present study we include the following two-body channels: ${}^3\text{H}(\frac{1}{2}^{+})+p$, ${}^3\text{He}(\frac{1}{2}^{+})+n$, $d(1^{+})+d(1^{+})$, $pn(0^{+})+pn(0^{+})$, and $pp(0^{+})+nn(0^{+})$. Here, for example, ${}^3\text{H}(\frac{1}{2}^{+})$ stands for not only the ground state of ${}^3\text{H}$ but also its excited states. The latter are actually unbound, and these configurations together with the ground-state wave function are obtained by diagonalizing the intrinsic Hamiltonian for the $p+n+n$ system in \mathcal{L}^2 basis functions. Similarly $pn(0^{+})$, $pp(0^{+})$, and $nn(0^{+})$ stand for the two-nucleon pseudo states with the isospin $T = 1$.

The total wave function $\Psi^{JM\pi}$ may be expressed in terms of a combination of various components, $\sum_{\text{AB}} \Psi_{\text{AB}}^{JM\pi}$, with

$$\Psi_{\text{AB}}^{JM\pi} = \sum_{i=1}^{N_A} \sum_{j=1}^{N_B} \sum_{I,\ell} \mathcal{A}[[\Phi_{J_A \pi_A}^{\text{A},i} \Phi_{J_B \pi_B}^{\text{B},j}]_I \chi_c]_{JM}, \quad (14)$$

where e.g. N_A is the basis size for the nucleus A, $\Phi_{J_A \pi_A}^{\text{A},i}$ is the intrinsic wave function of its i th state with the angular momentum J_A and the parity π_A , and χ_c is the relative motion function between the two nuclei. The angular momenta of the two nuclei are coupled to the channel spin I , which is further coupled with the partial wave ℓ for the relative motion to the total angular momentum JM . The index c denotes a set of (i, j, I, ℓ) . The parity π of the total wave function is $\pi_A \pi_B (-1)^{\ell}$.

In the MRM the configuration space is divided into two regions, internal and external, by a channel radius. The total wave function in the internal region, $\Psi_{\text{int}}^{JM\pi}$, is constructed by expanding $\chi_c(\mathbf{r})$ in terms of $r^{\ell} \exp(-\rho r^2) Y_{\ell}(\hat{\mathbf{r}})$ with a suitable set of ρ , while the total wave function in the external region, $\Psi_{\text{ext}}^{JM\pi}$, is represented by expressing χ_c with Coulomb or Whittaker functions depending on whether the channel is open or not. The scattering wave function and the S -matrix are determined by solving a Schrödinger equation

$$[H - E + \widetilde{L}] \Psi_{\text{int}}^{JM\pi} = \widetilde{L} \Psi_{\text{ext}}^{JM\pi} \quad (15)$$

in the internal region together with the continuity condition $\Psi_{\text{int}}^{JM\pi} = \Psi_{\text{ext}}^{JM\pi}$ at the channel radius. Here \widetilde{L} is the Bloch operator. See Ref. [21] for detail.

In the MRM the ground-state wave function of ${}^4\text{He}$ is approximated in combinations of the multi-channel configurations.

III. MODEL

A. Hamiltonian

The Hamiltonian we use reads

$$H = \sum_i T_i - T_{\text{cm}} + \sum_{i<j} v_{ij} + \sum_{i<j<k} v_{ijk}. \quad (16)$$

The kinetic energy of the center of mass motion is subtracted and the two-nucleon interaction v_{ij} consists of nuclear and Coulomb parts. As the NN potential we employ Argonne $v8'$ (AV8') [31] and G3RS [32] potentials that contain central, tensor and spin-orbit components. The \mathbf{L}^2 and $(\mathbf{L} \cdot \mathbf{S})^2$ terms in the G3RS potential are omitted. The NN potential of AV8' type contains eight pieces: $v_{ij} = \sum_{p=1}^8 v^{(p)}(r_{ij}) \mathcal{O}_{ij}^{(p)}$, where $v^{(p)}(r_{ij})$ and $\mathcal{O}_{ij}^{(p)}$ are the radial form factor and the operator characterizing each piece of the potential. The operators are defined as $\mathcal{O}_{ij}^{(1)} = 1$, $\mathcal{O}_{ij}^{(2)} = \boldsymbol{\sigma}_i \cdot \boldsymbol{\sigma}_j$, $\mathcal{O}_{ij}^{(3)} = \boldsymbol{\tau}_i \cdot \boldsymbol{\tau}_j$, $\mathcal{O}_{ij}^{(4)} = \boldsymbol{\sigma}_i \cdot \boldsymbol{\sigma}_j \boldsymbol{\tau}_i \cdot \boldsymbol{\tau}_j$, $\mathcal{O}_{ij}^{(5)} = S_{ij}$, $\mathcal{O}_{ij}^{(6)} = S_{ij} \boldsymbol{\tau}_i \cdot \boldsymbol{\tau}_j$, $\mathcal{O}_{ij}^{(7)} = (\mathbf{L} \cdot \mathbf{S})_{ij}$, $\mathcal{O}_{ij}^{(8)} = (\mathbf{L} \cdot \mathbf{S})_{ij} \boldsymbol{\tau}_i \cdot \boldsymbol{\tau}_j$, where S_{ij} is the tensor operator, and $(\mathbf{L} \cdot \mathbf{S})_{ij}$ is the spin-orbit operator. For the sake of later convenience, we define V_p by

$$V_p = \sum_{i<j} v^{(p)}(r_{ij}) \mathcal{O}_{ij}^{(p)}. \quad (17)$$

The AV8' potential is more repulsive at short distances and has a stronger tensor component than the G3RS potential. Due to this property one has to perform calculations of high accuracy particularly when the AV8' potential is used, in order to be safe from those problems of the CSM that are raised by Witała and Glöckle [33]. To reproduce the two- and three-body threshold energies is vital for a realistic calculation of $\sigma_\gamma(E_\gamma)$. To this end we add a three-nucleon force (3NF) v_{ijk} , and adopt a purely phenomenological potential [34] that is determined to fit the inelastic electron form factor from the ground state to the first excited state of ${}^4\text{He}$ as well as the binding energies of ${}^3\text{H}$, ${}^3\text{He}$ and ${}^4\text{He}$.

B. Gaussian basis functions

Basis functions defined here can apply to any number N of nucleons. The basis function we use for N -nucleon system takes a general form in LS coupling scheme

$$\Phi_{(LS)JM T M_T}^{(N)\pi} = \mathcal{A} \left[\phi_L^{(N)\pi} \chi_S^{(N)} \right]_{JM} \eta_{T M_T}^{(N)}, \quad (18)$$

where \mathcal{A} is the antisymmetrizer. We define spin functions by a successive coupling of each spin function $\chi_{\frac{1}{2}}(i)$

$$\begin{aligned} & \chi_{S_{12} S_{123} \dots S M_S}^{(N)} \\ & = [\dots [\chi_{\frac{1}{2}}(1) \chi_{\frac{1}{2}}(2)]_{S_{12}} \chi_{\frac{1}{2}}(3)]_{S_{123}} \dots]_{S M_S}. \end{aligned} \quad (19)$$

Since taking all possible intermediate spins (S_{12}, S_{123}, \dots) forms a complete set for a given S , any spin function $\chi_S^{(N)}$ can be expanded in terms of the functions (19). Similarly the isospin function $\eta_{T M_T}^{(N)}$ can also be expanded using a set of isospin functions $\eta_{T_{12} T_{123} \dots T M_T}^{(N)}$. In the MRM calculation we use a particle basis that in general contains a mixing of the total isospin T , which is caused by the Coulomb potential.

There is no complete set that is flexible enough to describe the spatial part $\phi_L^{(N)\pi}$. For example, harmonic-oscillator functions are quite inconvenient to describe spatially extended configurations. We use an expansion in terms of correlated Gaussians [17, 18]. As demonstrated in Ref. [35], the Gaussian basis leads to accurate solutions for few-body bound states interacting with the realistic NN potentials.

Two types of Gaussians are used. One is a basis expressed in a partial wave expansion

$$\begin{aligned} & \phi_{\ell_1 \ell_2 (L_{12}) \ell_3 (L_{123}) \dots L M_L}^{(N)\pi}(a_1, a_2, \dots, a_{N-1}) \\ & = \exp(-a_1 x_1^2 - a_2 x_2^2 - \dots - a_{N-1} x_{N-1}^2) \\ & \quad \times [\dots [\mathcal{Y}_{\ell_1}(\mathbf{x}_1) \mathcal{Y}_{\ell_2}(\mathbf{x}_2)]_{L_{12}} \mathcal{Y}_{\ell_3}(\mathbf{x}_3)]_{L_{123}} \dots]_{L M_L} \end{aligned} \quad (20)$$

with

$$\mathcal{Y}_\ell(\mathbf{r}) = r^\ell Y_\ell(\hat{\mathbf{r}}). \quad (21)$$

Here the coordinates $\mathbf{x}_1, \mathbf{x}_2, \dots, \mathbf{x}_{N-1}$ are a set of relative coordinates. The angular part is represented by successively coupling the partial wave ℓ_i associated with each coordinate. The values of a_i and ℓ_i as well as the intermediate angular momenta L_{12}, L_{123}, \dots are variational parameters. The angular momentum ℓ_i is limited to $\ell_i \leq 2$ in the present calculation. This basis is employed to construct the internal wave function $\Psi_{\text{int}}^{J M \pi}$ of the MRM calculation.

The other is an explicitly correlated Gaussian with a global vector representation [14, 17, 18, 20]

$$\begin{aligned} & \phi_{L_1 L_2 (L_{12}) L_3 L M_L}^{(N)\pi}(A, u_1, u_2, u_3) \\ & = \exp(-\tilde{\mathbf{x}} A \mathbf{x}) [\mathcal{Y}_{L_1}(\tilde{u}_1 \mathbf{x}) \mathcal{Y}_{L_2}(\tilde{u}_2 \mathbf{x})]_{L_{12}} \mathcal{Y}_{L_3}(\tilde{u}_3 \mathbf{x})]_{L M_L}, \end{aligned} \quad (22)$$

where A is an $(N-1) \times (N-1)$ positive definite symmetric matrix and u_i is an $(N-1)$ -dimensional column vector. Both A and u_i are variational parameters. The tilde symbol denotes a transpose, that is, $\tilde{\mathbf{x}} A \mathbf{x} = \sum_{i,j=1}^{N-1} A_{ij} \mathbf{x}_i \cdot \mathbf{x}_j$ and $\tilde{u}_i \mathbf{x} = \sum_{k=1}^{N-1} (u_i)_k \mathbf{x}_k$. The latter specifies the global vector u_i responsible for the rotation. The basis function (22) will be used in the CSM calculation. Actually a choice of the angular part of Eq. (22) is here restricted to $L_3 = 0$. With the two global vectors any L^π states but 0^- can be constructed with a suitable choice of L_1 and L_2 .

Apparently the basis function (22) includes correlations among the nucleons through the non-vanishing off

TABLE I: Ground-state properties of ${}^3\text{H}$ and ${}^4\text{He}$ calculated with the correlated Gaussians (22) using the AV8' and G3RS potentials together with 3NF. Here E , $\sqrt{\langle r_p^2 \rangle}$, and $\sqrt{\langle r_{pp}^2 \rangle}$ denote the energy, the root-mean-square radius of proton distribution and the root-mean-square relative distance of protons, respectively, and $P(L, S)$ stands for the probability (in %) of finding the component with the total orbital angular momentum L and the spin S . The experimental energy of ${}^4\text{He}$ is -28.296 MeV and the point proton radius is $1.457(14)$ fm [37].

	AV8'+3NF		G3RS+3NF	
	${}^3\text{H}$	${}^4\text{He}$	${}^3\text{H}$	${}^4\text{He}$
E (MeV)	-8.41	-28.43	-8.35	-28.56
$\sqrt{\langle r_p^2 \rangle}$ (fm)	1.70	1.45	1.74	1.47
$\sqrt{\langle r_{pp}^2 \rangle}$ (fm)	-	2.41	-	2.45
$P(0, 0)$	91.25	85.56	92.85	88.33
$P(2, 2)$	8.68	14.07	7.10	11.42
$P(1, 1)$	0.07	0.37	0.05	0.25

diagonal elements of A . Contrary to this, the basis function (20) takes a product form of a function depending on each coordinate, so that the correlation is usually accounted for by including the so-called rearrangement channels that are described with different coordinate sets [36]. A great advantage of Eq. (22) is that it keeps its functional form under the coordinate transformation. Hence one needs no such rearrangement channels but can use just one particular coordinate set, which enables us to calculate Hamiltonian matrix elements in a unified way. See Refs. [14, 20] for details.

The variational parameters are determined by the stochastic variational method [17, 18]. It is confirmed that both types of basis functions produce accurate results for the ground-state properties of ${}^3\text{H}$, ${}^3\text{He}$, and ${}^4\text{He}$ [14]. Table I lists the properties of ${}^3\text{H}$ and ${}^4\text{He}$ obtained using the basis (22). Included L_1 and L_2 values are the same as those used in Refs. [13, 14]. Both potentials of AV8'+3NF and G3RS+3NF reproduce the binding energy and the root-mean square radius of ${}^4\text{He}$ satisfactorily. The G3RS+3NF potential gives a slightly larger radius and a smaller D -state probability $P(2, 2)$ than the AV8'+3NF potential.

C. Two- and three-body decay channels

As is well-known, the electric dipole operator

$$\begin{aligned}
 \mathcal{M}_{1\mu} &= \sum_{i=1}^4 \frac{e}{2} (1 - \tau_{3i})(\mathbf{r}_i - \mathbf{x}_4)_\mu \\
 &= -\frac{e}{2} \sqrt{\frac{4\pi}{3}} \sum_{i=1}^4 \tau_{3i} \mathcal{Y}_{1\mu}(\mathbf{r}_i - \mathbf{x}_4) \\
 &= \frac{e}{2} \sqrt{\frac{4\pi}{3}} \left\{ \frac{1}{2} (\tau_{31} - \tau_{32}) \mathcal{Y}_{1\mu}(\mathbf{x}_1) \right. \\
 &\quad + \frac{1}{3} (\tau_{31} + \tau_{32} - 2\tau_{33}) \mathcal{Y}_{1\mu}(\mathbf{x}_2) \\
 &\quad \left. + \frac{1}{4} (\tau_{31} + \tau_{32} + \tau_{33} - 3\tau_{34}) \mathcal{Y}_{1\mu}(\mathbf{x}_3) \right\} \quad (23)
 \end{aligned}$$

is an isovector, where \mathbf{x}_4 is the center of mass coordinate of ${}^4\text{He}$, and \mathbf{x}_i is the Jacobi coordinate: $\mathbf{x}_1 = \mathbf{r}_2 - \mathbf{r}_1$, $\mathbf{x}_2 = \mathbf{r}_3 - \frac{1}{2}(\mathbf{r}_1 + \mathbf{r}_2)$, $\mathbf{x}_3 = \mathbf{r}_4 - \frac{1}{3}(\mathbf{r}_1 + \mathbf{r}_2 + \mathbf{r}_3)$. This operator excites the ground state of ${}^4\text{He}$ to those states that have $J^\pi T = 1^- 1$ in so far as a small isospin admixture in the ground state of ${}^4\text{He}$ is ignored. Moreover those excited states should mainly have $(L, S) = (1, 0)$ component, because the ground state of ${}^4\text{He}$ is dominated by the $(0, 0)$ component. See Table I. Excited states with $S = 1$ or 2 components will be weakly populated by the $E1$ transition through the minor components (12–14%) of the ${}^4\text{He}$ ground state.

According to the R -matrix phenomenology as quoted in Ref. [38], two levels with $1^- 1$ are identified. Their excitation energies and widths in MeV are respectively $(E_x, \Gamma) = (23.64, 6.20)$, $(25.95, 12.66)$. We have recently studied the level structure of ${}^4\text{He}$ and succeeded to reproduce all the known levels below 26 MeV [13]. With including the 3NF, two $1^- 1$ states are predicted at about 23 and 27 MeV in case of the AV8' potential. They are however not clearly identified as resonances in a recent microscopic scattering calculation [20]. In Sec. IV A, we will show that three states with strong $E1$ strength are obtained below 35 MeV in a diagonalization using the \mathcal{L}^2 basis and will discuss the properties of those states.

Low-lying excited states with $1^- 1$ decay to ${}^3\text{H}+p$ and ${}^3\text{He}+n$ channels with P wave. Possible channel spins $2^{l+1}\ell_j$ that the ${}^3\text{H}+p$ or ${}^3\text{He}+n$ continuum state takes are 1P_1 and 3P_1 [20]. A main component of the 1P_1 continuum state is found to be $(L, S) = (1, 0)$ while that of the 3P_1 continuum state is $(1, 1)$. Thus it is expected that the $E1$ excitation of ${}^4\text{He}$ is followed mainly by the ${}^3\text{H}+p$ and ${}^3\text{He}+n$ decays in the 1P_1 channel, which agrees with the result of a resonating group method calculation including the ${}^3\text{H}+p$, ${}^3\text{He}+n$, and $d+d$ physical channels [7].

The two-body decay to $d+d$ is suppressed due to the isospin conservation. Above the $d+p+n$ threshold at 26.07 MeV, this three-body decay becomes possible where the decaying pn pair is in the $T = 1$ state. In fact the cross section to this three-body decay is observed experimentally [1].

D. Square-integrable basis with $J^\pi T = 1^- 1$

The accuracy of the CSM calculation crucially depends on how sufficiently the \mathcal{L}^2 basis functions $\Phi_i(\mathbf{x})$ for $J^\pi T = 1^- 1$ are prepared for solving the eigenvalue problem (9). We attempt at constructing the basis paying attention to two points: the sum rule of $E1$ strength and the decay channels as discussed in Sec. III C. As the $E1$ operator (23) suggests, we will construct the basis with 1^- by choosing the following three operators and acting them on the basis functions that constitute the ground state of ${}^4\text{He}$: (i) a single-particle excitation built with $\mathcal{Y}_{1\mu}(\mathbf{r}_1 - \mathbf{x}_4)$, (ii) a $3N+N$ (${}^3\text{H}+p$ and ${}^3\text{He}+n$) two-body disintegration due to $\mathcal{Y}_{1\mu}(\mathbf{x}_3)$, (iii) a $d+p+n$ three-body disintegration due to $\mathcal{Y}_{1\mu}(\mathbf{x}_2)$. See Fig. 1. The basis (i) is useful for satisfying the sum rule, and the bases (ii) and (iii) take care of the two- and three-body decay asymptotics. These cluster configurations will be better described using the relevant coordinates rather than the single-particle coordinate. It should be noted that the classification label does not necessarily indicate strictly exclusive meanings because the basis functions belonging to the different classes have some overlap among others because of their non-orthogonality.

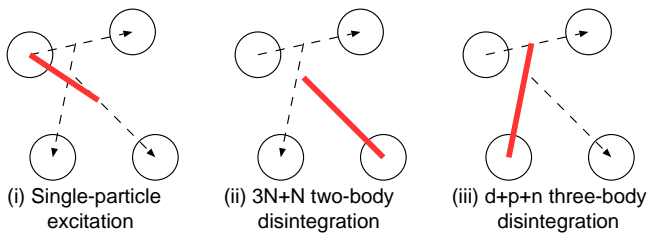


FIG. 1: (Color online) Three patterns for the dipole excitations for ${}^4\text{He}$. Thick solid lines denote the coordinates on which the spatial part of the $E1$ operator acts.

We will slightly truncate the ground-state wave functions of ${}^3\text{H}$, ${}^3\text{He}$, and ${}^4\text{He}$ when they are needed to construct the above 1^- configurations, (i) and (ii). With this truncation a full calculation presented in Sec. IV will be possible without excessive computer time. As shown in Table I, the ground states of these nuclei contain a small amount (less than 0.5%) of $L = 1$ component, so that we omit this component and reconstruct the ground-state wave functions using only with $L_1=0, 2$ and $L_2 = L_3 = 0$ in Eq. (22). The energy loss is found to be small compared to the accurate energy of Table I. E.g., in the case of AV8'+3NF, the loss is 0.23 MeV for ${}^3\text{H}$ in 64 basis dimension and 1.53 MeV for ${}^4\text{He}$ in 200 basis dimension. The truncated ground-state wave function is denoted $\Psi_{\frac{1}{2}M\frac{1}{2}M_T}^{(3)}$ for $3N$ and $\Psi_{0000}^{(4)}$ for ${}^4\text{He}$.

Note, however, that we use the accurate wave function Ψ_0 of Table I for the ${}^4\text{He}$ ground state in computing $S(E)$ with Eq. (11).

1. Single-particle (sp) excitation

As is well-known, applying the $E1$ operator on a ground state leads to a coherent state that exhausts all the $E1$ strength from the ground state. The coherent state is however not an eigenstate of the Hamiltonian. In analogy to this, the basis of type (i) is constructed as follows

$$\Psi_f^{\text{sp}} = \mathcal{A} \left[\Phi_0^{(4)}(i) \mathcal{Y}_1(\mathbf{r}_1 - \mathbf{x}_4) \right]_{1M} \eta_{T_{12}T_{123}}^{(4)}, \quad (24)$$

where $\Phi_0^{(4)}(i)$ is the space-spin part of the i th basis function of $\Psi_{0000}^{(4)}$. We include all the basis functions and all possible T_{12}, T_{123} for the four-nucleon isospin state with $TM_T=10$. The truncated basis $\Phi_0^{(4)}(i)$ consists of either $[\phi_0^{(4)+} \chi_0^{(4)}]_0$ or $[\phi_2^{(4)+} \chi_2^{(4)}]_0$ in the notation of Eq. (18). The former contains no global vector, while the latter contains one global vector. Since $\mathcal{Y}_1(\mathbf{r}_1 - \mathbf{x}_4)$ is rewritten as $\mathcal{Y}_1(\tilde{w}\mathbf{x})$ with $\tilde{w} = (-\frac{1}{2}, -\frac{1}{3}, -\frac{1}{4})$, the basis (24) contains at most two global vectors and reduces to the correlated Gaussian (22). For example, the basis with the latter case can be reduced, after the angular momentum recoupling, to the standard form with $L_1 = 2, L_2 = 1$

$$\begin{aligned} & \left[[\phi_{20(2)02}^{(4)+}(A, u_1) \chi_{1\frac{3}{2}2}^{(4)}]_0 \mathcal{Y}_1(\mathbf{r}_1 - \mathbf{x}_4) \right]_{1M} \\ &= \sum_{L_{12}=1,2,3} \sqrt{\frac{2L_{12}+1}{15}} \left[\phi_{21(L_{12})0L_{12}}^{(4)-}(A, u_1, w) \chi_{1\frac{3}{2}2}^{(4)} \right]_{1M}. \end{aligned} \quad (25)$$

Each L_{12} component of $[\phi_{21(L_{12})0L_{12}}^{(4)-}(A, u_1, w) \chi_{1\frac{3}{2}2}^{(4)}]_{1M}$ is included as an independent basis function in what follows.

2. $3N+N$ two-body disintegration

In this basis the nucleon couples with the ground and pseudo states of the $3N$ system. Their relative motion carries P -wave excitations, and it is described in a combination of several Gaussians. The basis function takes the following form

$$\begin{aligned} \Psi_f^{3\text{NN}} &= \mathcal{A} \left[\Phi_{J_3}^{(3)}(i) \exp(-a_3 x_3^2) [\mathcal{Y}_1(\mathbf{x}_3) \chi_{\frac{1}{2}}^{(4)}(4)]_j \right]_{1M} \\ &\quad \times [\eta_{T_{12}\frac{1}{2}}^{(3)} \eta_{\frac{1}{2}}^{(4)}(4)]_{10}, \end{aligned} \quad (26)$$

where $\Phi_{J_3}^{(3)}(i)$ is the space-spin part of the i th basis function of $\Psi_{\frac{1}{2}M\frac{1}{2}M_T}^{(3)}$. The value of j takes $\frac{1}{2}$ and $\frac{3}{2}$, and J_3 takes any of $\frac{1}{2}, \frac{3}{2}$, and $\frac{5}{2}$ that, with j , can add up to the angular momentum 1. The parameter a_3 is taken in a geometric progression as $12.5/1.4^{2(k-1)}$ ($k = 1, 2, \dots, 15$) in fm^{-2} . As in the basis of the single-particle excitation the space-spin part is again expressed in the correlated Gaussians (22) with at most two global vectors, where one of

the global vectors is $\mathcal{Y}_1(\mathbf{x}_3)=\mathcal{Y}_1(\tilde{w}\mathbf{x})$ with $\tilde{w}=(0,0,1)$. All the basis states with different values of J_3 and j are included independently.

3. $d+p+n$ three-body disintegration

In this basis the relative motion between $3N$ and N is S wave but the $3N$ system is excited to the $d+N$ configuration with P -wave relative motion. Here d does not necessarily mean its ground state but include pseudo states with the angular momentum $J_2^\pi = 0^+, 1^+, 2^+, 3^+$. The spatial part is however taken from the basis functions of the deuteron ground state. The three-body basis function takes the following form

$$\Psi_f^{\text{d}p\text{n}} = \mathcal{A} \left[\Phi_{J_3}^{(\text{d}N)}(i) \exp(-a_3 x_3^2) [\mathcal{Y}_0(\mathbf{x}_3) \chi_{\frac{1}{2}}(4)]_{\frac{1}{2}} \right]_{1M} \times [\eta_0^{(3)}(123) \eta_{\frac{1}{2}}(4)]_{10}, \quad (27)$$

with

$$\Phi_{J_3}^{(\text{d}N)}(i) = \left[\Psi_{J_2}^{(2)}(i) \exp(-a_2 x_2^2) [\mathcal{Y}_1(\mathbf{x}_2) \chi_{\frac{1}{2}}(3)]_j \right]_{J_3}, \quad (28)$$

where $\Psi_{J_2}^{(2)}(i)$ is the (pseudo) deuteron wave function mentioned above. Both of J_3 and j take $\frac{1}{2}$ and $\frac{3}{2}$. All possible sets of J_3 , J_2 and j values that satisfy the angular momentum addition rule are included in the calculation. Both a_2 and a_3 are again given in a geometric progression, $3.125/1.4^{2(k-1)}$ ($k=1, 2, \dots, 10$) in fm^{-2} . Note that $\mathcal{Y}_1(\mathbf{x}_2)=\mathcal{Y}_1(\tilde{w}\mathbf{x})$ with $\tilde{w}=(0,1,0)$. After recoupling the orbital and spin angular momenta, the basis (27) leads to the following space-spin parts: $[\phi_{L_1 1(L)0L}^{(4)-} \chi_{1S_{123}S}^{(4)}]_{1M}$ with $L_1=0$ or 2 , and all possible values of L , S_{123} , S are allowed. These are included independently. Note that the matrix A of $\phi_{L_1 1(L)0L}^{(4)-}$ becomes diagonal.

The basis dimension included is 7400 (7760) for AV8'+3NF (G3RS)+3NF, 1200 (1560) from (i), 3000 from (ii), and 3200 from (iii), respectively.

IV. RESULTS

A. Discretized strength of electric dipole transition

Continuum states with $J^\pi T = 1^- 1$ are discretized by diagonalizing the Hamiltonian in the basis functions defined in Sec. III. These discretized states provide us with an approximate distribution of the $E1$ strength. Figure 2 displays the reduced transition probability

$$B(E1, \lambda) = \sum_{M\mu} \left| \langle \Psi_\lambda^{1M-}(\theta=0) | \mathcal{M}_{1\mu} | \Psi_0 \rangle \right|^2. \quad (29)$$

as a function of the discretized energy $E_\lambda(\theta=0)$. The calculations were performed in each basis set of (i)–(iii)

as well as a full basis that includes all of them. The distribution of $B(E1, \lambda)$ depends rather weakly on the potentials.

As expected, three types of basis functions play a distinctive and supplementary role in the $E1$ strength distribution. The basis functions (i) produce strongly concentrated strength at about 27 MeV and another peak above 40 MeV. The $(L, S) = (1, 0)$ component of these states is about 95%. With the $3N+N$ two-body configurations (ii), we obtain two peaks in the region of 20–30 MeV and one or two peaks at around 35 MeV. The two peaks at about 25 MeV may perhaps correspond to the 1^- levels with $T=1$ at 23.64 and 25.95 MeV with very broad widths [38]. Note, however, that a microscopic four-nucleon scattering calculation presents no conspicuous resonant phase shifts for 3P_1 and 1P_1 channels [20]. The three-body configurations (iii) give relatively small strength broadly in the excitation energy above 30 MeV. The three prominent peaks at around 25–35 MeV remain to exist in the full basis calculation. This implies that the low-lying strength mainly comes from the $3N+N$ configuration. We will return this issue in Sec. IV D. The three discretized states are labeled by their excitation energies E_i in what follows.

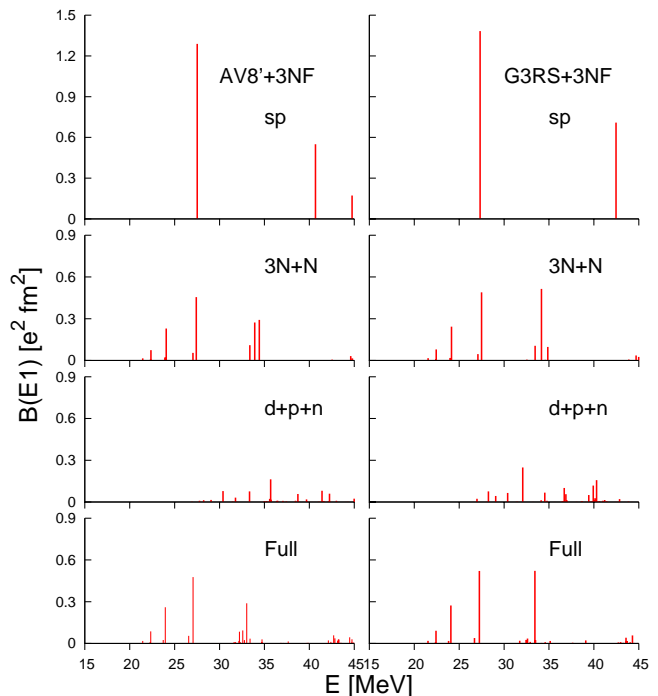


FIG. 2: (Color online) Discretized strength of the $E1$ transitions in ${}^4\text{He}$. See the text for the calculations classified by sp , $3N+N$, $d+p+n$, and Full.

Table II shows the properties of the three states E_i that have strong strength. The expectation value of each piece of the Hamiltonian is a measure of its contribution to the energy. We see that the central ($V_4: \sigma_i \cdot \sigma_j \tau_i \cdot \tau_j$) and tensor ($V_6: S_{ij} \tau_i \cdot \tau_j$) terms are major contributors

among the interaction pieces. The one-pion exchange potential (OPEP) consists of V_6 and V_4 terms, so that the tensor force of the OPEP is found to play a vital role. The value of $P(L, S)$ in the table is obtained by the squared coefficient $(C_{LS}^\lambda)^2$ of the expansion

$$\Psi_\lambda^{1M^-}(\theta = 0) = \sum_{LS} C_{LS}^\lambda \Psi_{(LS)1M10}^{(4)-}, \quad (30)$$

where $\Psi_{(LS)1M10}^{(4)-}$ is normalized. Note that no basis functions with $L^\pi = 0^-$ are included in the present calculation as they are not expressible in the two global vectors. As expected, all of the three states dominantly consist of the $(1, 0)$ component, which can be excited, by the $E1$ operator, from the main component $(0, 0)$ of the ${}^4\text{He}$ ground state. We see a considerable admixture of the $S = 2$ components especially with $L = 3$ in the three states. This is understood from the role played by the tensor force that couples the $S = 0$ and 2 states. In fact the $S = 2$ states lose energy due to large kinetic energy contributions but gain energy owing to the coupling with the main component with $(1, 0)$ through the tensor force. For example, in the case of E_1 state, the diagonal matrix elements of the kinetic energy, $\langle \Psi_{(L2)1M10}^{(4)-} | T | \Psi_{(L2)1M10}^{(4)-} \rangle$, are 196.5 (160.3), 198.6 (161.5), 199.3 (162.3) MeV for $L=1, 2, 3$ with AV8' (G3RS)+3NF, while the tensor coupling matrix elements between $(1, 0)$ and $(L, 2)$ states, $\langle \Psi_{(10)1M10}^{(4)-} | V_5 + V_6 | \Psi_{(L2)1M10}^{(4)-} \rangle$, are respectively -54.5 (-40.2), -70.8 (-52.1), -84.0 (-61.9) MeV for $L=1, 2, 3$ states.

The $E1$ transition density is defined as

$$\rho_\lambda(r) = \langle \Psi_\lambda^{10^-}(\theta = 0) | \sum_{i=1}^4 \frac{\delta(|\mathbf{r}_i - \mathbf{x}_4| - r)}{r^2} \times \mathcal{Y}_{10}(\mathbf{r}_i - \mathbf{x}_4) \frac{1 - \tau_{3i}}{2} | \Psi_0 \rangle, \quad (31)$$

which gives the $E1$ transition matrix element through

$$\langle \Psi_\lambda^{10^-}(\theta = 0) | \mathcal{M}_{10} | \Psi_0 \rangle = \sqrt{\frac{4\pi}{3}} e \int_0^\infty \rho_\lambda(r) r^2 dr. \quad (32)$$

Figure 3 displays the transition densities for the three states E_i of Table II that give the large $E1$ matrix elements. The dependence of the transition density on the interaction is rather weak except for the third state labeled by E_3 . The transition density extends to significantly large distances mainly due to the effect of the $3N+N$ configurations, so that for a reliable evaluation of $B(E1, \lambda)$ the basis functions for 1^- must include configurations that reach far distances. The peak of $r^2\rho_\lambda(r)$ appears at about 2 fm, which is much larger than the peak position (1.1 fm) of $r^2\rho_{\text{g.s.}}(r)$, where $\rho_{\text{g.s.}}(r)$ is the ground-state density of ${}^4\text{He}$. A comparison of the transition densities of the second (E_2) and third (E_3) states suggests that near $r \approx 2-6$ fm they exhibit a constructive pattern in the second state and a destructive pattern in the third state.

TABLE II: Properties of the three 1^- states that exhibit strong $B(E1)$ strength. The excitation energy E and the expectation values are given in units of MeV. The value of $P(L, S)$ is given in %. See Table I for the ground-state energy of ${}^4\text{He}$.

E	AV8'+3NF			G3RS+3NF		
	23.96	27.05	33.02	24.08	27.25	33.43
$\langle H \rangle$	-4.46	-1.38	4.60	-4.48	-1.31	4.88
$\langle T \rangle$	51.21	54.78	43.71	44.34	48.37	49.65
$\langle V_1 \rangle$	6.42	6.37	4.44	-0.14	-0.24	-0.31
$\langle V_2 \rangle$	-3.41	-3.68	-1.61	-3.07	-3.38	-2.94
$\langle V_3 \rangle$	-2.17	-2.15	-1.65	-3.81	-3.75	-3.43
$\langle V_4 \rangle$	-23.83	-24.04	-16.09	-20.45	-20.81	-18.46
$\langle V_5 \rangle$	0.22	0.22	0.14	-0.41	-0.41	-0.37
$\langle V_6 \rangle$	-30.60	-30.51	-22.71	-20.60	-20.64	-18.80
$\langle V_7 \rangle$	4.79	4.77	3.55	2.33	2.33	2.13
$\langle V_8 \rangle$	-6.76	-6.73	-4.96	-2.37	-2.38	-2.15
$\langle V_{3\text{NF}} \rangle$	-0.74	-0.86	-0.55	-0.72	-0.85	-0.85
$\langle V_{\text{Coul}} \rangle$	0.42	0.45	0.32	0.41	0.45	0.42
$P(1, 0)$	87.18	84.58	82.70	90.12	88.47	79.73
$P(1, 1)$	4.76	7.47	7.59	3.18	4.89	13.86
$P(2, 1)$	0.16	0.25	0.22	0.09	0.13	0.36
$P(1, 2)$	0.89	0.74	4.56	0.85	0.76	0.95
$P(2, 2)$	2.17	1.99	1.40	1.89	1.79	1.41
$P(3, 2)$	4.85	4.97	3.53	3.86	3.95	3.69

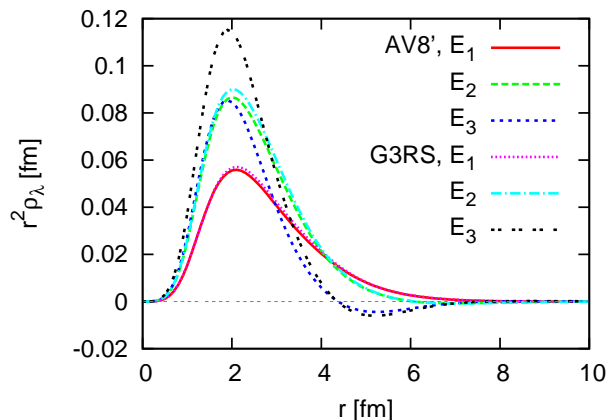


FIG. 3: (Color online) Transition densities for the three discretized states listed in Table II that have strong $E1$ strength.

B. Test of CSM calculation

The strength function (11) calculated in the CSM using the full basis is plotted in Fig. 4 for some angles θ . Both AV8'+3NF and G3RS+3NF potentials give similar results. With $\theta=10^\circ$, $S(E)$ shows some oscillations whose peaks appear at the energies of the discretized states shown in the full calculation of Fig. 2. To understand this behavior we note that the contribution of

an eigenstate λ to $S(E)$ is given by a Lorentz distribution

$$\frac{1}{\pi} \frac{1}{(E - E_c)^2 + \frac{1}{4}\Gamma_c^2} \sum_{\mu} \left[\frac{1}{2}\Gamma_c \text{Re}\tilde{\mathcal{D}}_{\mu}^{\lambda}(\theta)\mathcal{D}_{\mu}^{\lambda}(\theta) - (E - E_c)\text{Im}\tilde{\mathcal{D}}_{\mu}^{\lambda}(\theta)\mathcal{D}_{\mu}^{\lambda}(\theta) \right], \quad (33)$$

where $E_{\lambda}(\theta) = E_c - \frac{i}{2}\Gamma_c$. For small angles, E_c is not very different from the discretized energy $E_{\lambda}(\theta = 0)$ and Γ_c is small, and therefore the strength at $E \approx E_c$ comes mostly from the eigenstate λ alone because the contribution from the neighboring states can be neglected. The oscillatory behavior diminishes with increasing θ or Γ_c , and finally we obtain one broad peak at 26-27 MeV. As shown in the figure, the convergence reaches at about $\theta=17^{\circ}$. One might consider $\theta=17^{\circ}$ a little too small to cover the two 1^{-} states noted in Sec. III C. Attempting at including them by increasing θ will lead to numerically unstable and unphysical results particularly near the ${}^3\text{H}+p$ threshold with the present basis dimension. Though the strength should in principle vanish below the threshold energy, those eigenstates λ which have large values of Γ_c may contribute to the strength near the threshold and therefore it would be in general hard to obtain vanishing strength just below the threshold. After some trial and error calculations we choose $\theta=17^{\circ}$ as an acceptable angle hereafter.

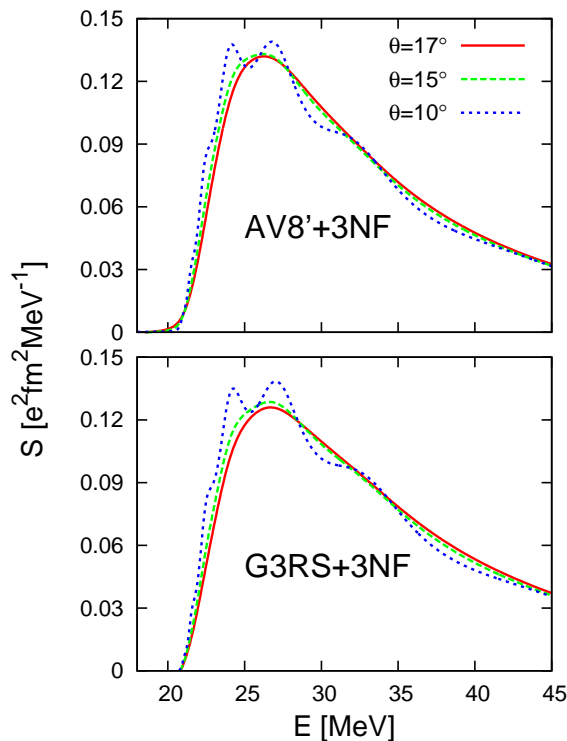


FIG. 4: (Color online) Electric dipole strength functions obtained by the CSM with different rotational angles θ .

Figure 5 compares the photoabsorption cross sections

$\sigma_{\gamma}(E_{\gamma})$ between the CSM and the MRM. The calculated ${}^3\text{H}+p$ threshold is adjusted to agree with experiment. As already mentioned, the $\sigma_{\gamma}(E_{\gamma})$ value of the MRM is defined as a sum of $\sigma_{\gamma}^{{}^3\text{H}p}(E_{\gamma})$ and $\sigma_{\gamma}^{{}^3\text{He}n}(E_{\gamma})$. Both methods give almost the same cross section, which convinces us of the validity of the CSM calculation. A little difference appears especially at the energy close to the threshold. We think that the reason for that is partly because the model space employed is not exactly the same each other, partly because the MRM calculation does not take into account the three- and four-body decay channels and partly because the CSM cross section may not be very accurate near the threshold energy as mentioned above.

A comparison of $\sigma_{\gamma}(E_{\gamma})$ between theory and experiment will be made in Sec. IV D.

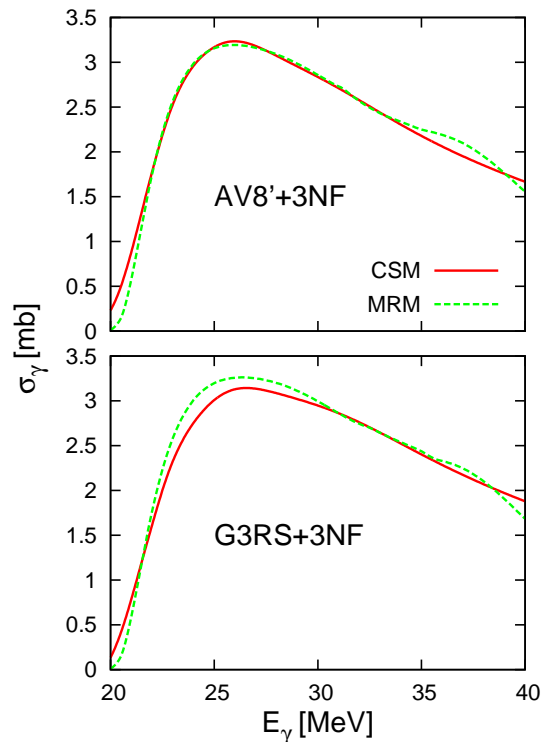


FIG. 5: (Color online) Comparison of the photoabsorption cross sections calculated with the CSM and the MRM.

C. Photonuclear sum rules

Photonuclear sum rules are related to the moments of different order of $\sigma_{\gamma}(E_{\gamma})$. The moment is defined as

$$m_p(E_{\text{max}}) = \int_0^{E_{\text{max}}} E_{\gamma}^p \sigma_{\gamma}(E_{\gamma}) dE_{\gamma}. \quad (34)$$

The moments m_0 , m_{-1} , and m_{-2} are called the Thomas-Reiche-Kuhn, bremsstrahlungs, and polarizability sum rules, respectively. These moments for $E_{\text{max}} \rightarrow \infty$ are

expressed with the ground-state expectation values of appropriate operators, and thus carry interesting electromagnetic properties of nuclei [39, 40]. As is well-known, they are expressed as

$$m_{-1}(\infty) = \mathcal{G} \left(Z^2 \langle r_p^2 \rangle - \frac{Z(Z-1)}{2} \langle r_{pp}^2 \rangle \right),$$

$$m_0(\infty) = \mathcal{G} \frac{3NZ\hbar^2}{2Am_N} (1 + K), \quad (35)$$

where $\mathcal{G} = 4\pi^2 e^2 / 3\hbar c$ and m_N is the nucleon mass. Here $\langle r_p^2 \rangle$ stands for the mean square radius of proton distribution and $\langle r_{pp}^2 \rangle$ for the mean square relative distance of protons. See Table I.

The enhancement factor K is given as a sum of the contributions from the potential pieces, $K = \sum_{p=1}^8 K_p$, where

$$K_p = \frac{2Am_N}{3NZ\hbar^2 e^2} \frac{1}{2} \sum_{\mu} \langle \Psi_0 | [\mathcal{M}_{1\mu}^\dagger, [V_p, \mathcal{M}_{1\mu}]] | \Psi_0 \rangle. \quad (36)$$

For the NN potential of AV8' type, K gains contributions from the potential piece with the $\tau_i \cdot \tau_j$ dependence, i.e., the charge-exchange interaction. The values of K_p are listed in Table III. For the sake of reference, we also show the expectation value $\langle V_p \rangle$ for the ground state of ${}^4\text{He}$. Roughly half of the respective total values, K and $\sum_p \langle V_p \rangle$, come from the tensor (V_6) and central (V_4) terms. Since the OPEP contains both V_6 and V_4 terms, it is instructive to know what values the OPEP predicts for $\langle V_p \rangle$ and K_p . The radial form factor $v^{(p)}(r)$ of the OPEP is made to vanish for $r \leq 1$ fm in order to estimate the role of the OPEP in the medium- and long-range parts of the NN interaction. As shown in Table III, the OPEP explains most of the contributions from the V_6 term. However, the OPEP is not enough to account for the V_4 contribution. Other central forces of V_4 type contribute in the medium-range part of the NN interaction.

The two large contributions originate from the matrix elements for the $(L, S) = (0,0) - (2,2)$ couplings and the $(0,0) - (0,0)$ diagonal channels, respectively. The AV8' potential has a stronger tensor component than the G3RS potential, predicting a slightly larger value for K . The present value of K is smaller than other calculations, e.g., 1.14 with the Reid soft core potential [41], 1.29 with the AV14+UVII potential [42], and 1.44 with the AV18+UIX potential [8].

The continuum discretized 1⁻1 states calculated with $\theta = 0^\circ$ satisfy the sum rule for $m_{-1}(\infty)$ almost perfectly: 99.6% for AV8'+3NF and 99.7% for G3RS+3NF. This implies that the present basis functions sufficiently span the configuration space needed to account for all the strengths of the $E1$ transition.

Figure 6 displays the convergence of the various moments with respect to the upper limit of the integration. It is surprising that even the moments calculated from the discretized states with $\theta = 0^\circ$ lead to a good

TABLE III: Contributions of the eight pieces V_p of the NN potential to the enhancement factor K and to the ground state energy of ${}^4\text{He}$ given in MeV. The values in parentheses are contributions of the OPEP that are calculated as explained in the text. The D -state probability of the deuteron is 5.77% for AV8' and 4.78% for G3RS.

p	AV8'+3NF		G3RS+3NF	
	$\langle V_p \rangle$	K_p	$\langle V_p \rangle$	K_p
1	17.39	0	1.07	0
2	-9.59	0	-8.75	0
3	-5.22	0.011	-9.11	0.059
4	-59.42	0.460	-51.80	0.474
	(-12.51)	(0.187)	(-12.50)	(0.191)
5	0.75	0	-0.93	0
6	-70.93	0.574	-47.16	0.484
	(-68.65)	(0.667)	(-59.37)	(0.610)
7	11.09	0	5.53	0
8	-15.93	0.061	-5.65	0.025
Total	-131.9	1.11	-116.8	1.04

approximation, already at $E_{\text{max}} = 60$ MeV, to the moments obtained with the CSM. The moment m_{-2} converges well at the rest energy of a pion, but the moment m_0 is still increasing beyond that energy. Our moments appear consistent with those calculated with the potential of Argonne $v18$ +UIX in the LIT method [8]. For $E_{\text{max}} = 135$ MeV we obtain $m_{-2} = 0.0710$ mb MeV⁻¹, $m_{-1} = 2.36$ mb (96% of $m_{-1}(\infty)$), and $m_0 = 92.0$ mb MeV (73% of $m_0(\infty)$) with AV8'+3NF, while the corresponding values with G3RS+3NF are 0.0725 mb MeV⁻¹, 2.45 mb (96% of $m_{-1}(\infty)$), and 97.1 mb MeV (80% of $m_0(\infty)$), respectively. We estimate the m_0 value for $E_{\text{max}} = 135$ MeV using the experimental cross sections [43]. The extracted value is 100 ± 5 mb MeV, which agrees fairly well with our theoretical values noted above. See also Fig. 11 later.

D. Comparison with experiment

We compare in Fig. 7 the photoabsorption cross sections for the reactions ${}^4\text{He}(\gamma, p){}^3\text{H}$ and ${}^4\text{He}(\gamma, n){}^3\text{He}$ between the MRM calculation and experiment. The calculated cross sections do not depend on the potentials up to about 25 MeV, and then the AV8'+3NF potential predicts slightly smaller values than the G3RS+3NF potential beyond the resonance peak. The MRM result for the (γ, p) cross section agrees rather well with the 1983 evaluation [44] as well as the very recent data [5], but disagrees with the data [1] in the low energy region. The ${}^4\text{He}(\gamma, n){}^3\text{He}$ cross section obtained in the MRM is much larger than that of the 1983 evaluation in the energy region of 25–35 MeV. The (γ, n) data are considerably scattered among the experiments. Compared to the recent data [2], the MRM result is consistent with

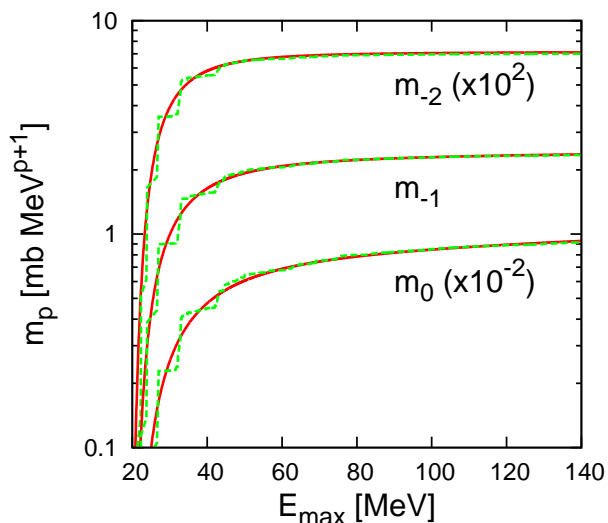


FIG. 6: (Color online) Moments of the photoabsorption cross section as a function of the upper limit of the integration. The moments with the discretized states ($\theta = 0^\circ$) are also plotted. The AV8'+3NF potential is used. Unit of m_p is mb MeV^{p+1} .

experiment in 25–28 MeV but is considerably larger than experiment in 30–40 MeV. The MRM cross sections of both (γ, p) and (γ, n) reactions agree fairly well with the new data [45] beyond 30 MeV. Compared to the LIT calculation [3] with the simple Malfliet-Tjon potential, our cross sections of both (γ, p) and (γ, n) are similar to their results that include final state interactions. It is noted that in our MRM calculation the peak height of the giant resonance is slightly lower and the resonance width is slightly broader than in the LIT calculation.

Figure 8 shows the cross section ratio of $\sigma_\gamma^{3\text{H}p}/\sigma_\gamma^{3\text{He}n}$, which is an important quantity to test the charge symmetry of the nuclear interaction. In the present calculation only the Coulomb potential breaks the charge symmetry. Both of the AV8'+3NF and G3RS+3NF potentials give virtually the same ratio. The calculated ratio is consistent with the recent measurements [1, 45, 46] as well as the theoretical calculations [3, 47]. It is interesting to note that the ratio of the data [1] agrees very well with our result though each of (γ, p) and (γ, n) cross sections is considerably smaller than our cross section. According to the 1983 evaluation [44] the ratio is as large as 1.5 in the 25–30 MeV region. We think it is probably attributed to the inefficiency of observing the cross section of ${}^4\text{He}(\gamma, n){}^3\text{He}$ compared to that of ${}^4\text{He}(\gamma, p){}^3\text{H}$. The rise of the ratio below 22 MeV is simply due to the difference between the ${}^3\text{H}+p$ and ${}^3\text{He}+n$ thresholds.

We display in Fig. 9 the total photoabsorption cross section $\sigma_\gamma(E_\gamma)$ calculated with the CSM. The two potentials give qualitatively the same results, but a careful look shows that the resonance energy and the width given by the AV8'+3NF potential are slightly smaller than those obtained with the G3RS+3NF potential. The calculation

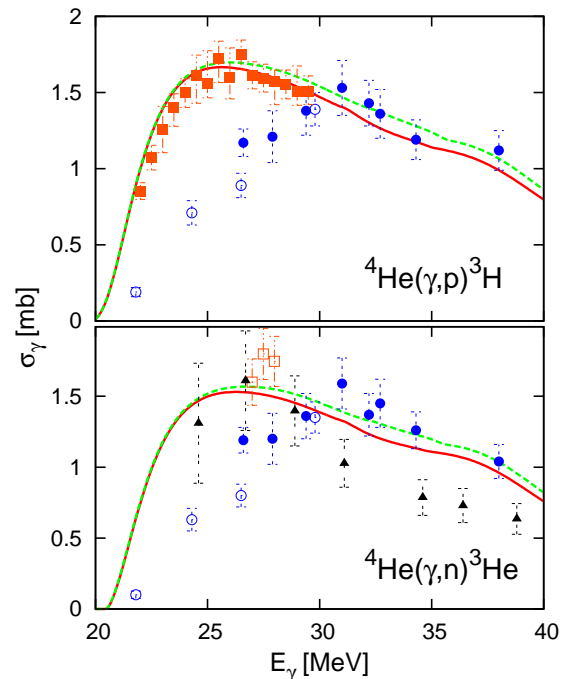


FIG. 7: (Color online) Photoabsorption cross sections of ${}^4\text{He}(\gamma, p){}^3\text{H}$ and ${}^4\text{He}(\gamma, n){}^3\text{He}$ reactions compared between the MRM calculation and experiment. Solid curve: AV8'+3NF; dashed curve: G3RS+3NF. The data are taken as follows: open circle [1], square [5], closed circle [45], and triangle [2].

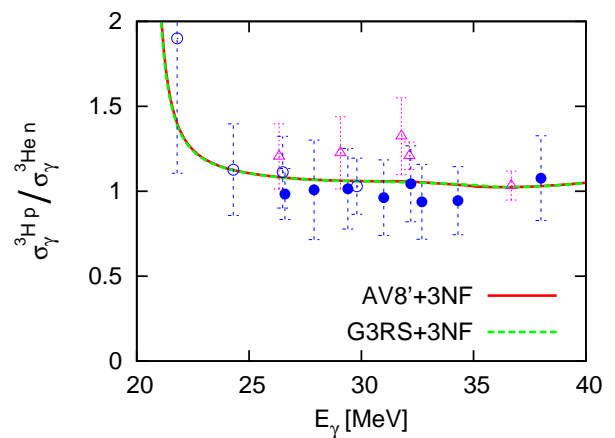


FIG. 8: (Color online) Ratio of the photoabsorption cross sections of ${}^4\text{He}(\gamma, p){}^3\text{H}$ and ${}^4\text{He}(\gamma, n){}^3\text{He}$. The data are taken as follows: open circle [1], closed circle [45], and triangle [46].

predicts a sharp rise of the cross section from the threshold, which is observed by several measurements [4, 43] but not in the data of Ref. [1]. Our result is consistent with the LIT calculations [10, 11] starting from the realistic interactions especially in the cross section near the threshold. It seems that the data [4, 45] indicate a small rise of the cross section at 31 MeV, but no such behavior

appears in the theory.

It is noted that the data of Ref. [4] appear to predict slightly smaller cross sections than our result though the shape of the cross section agrees well. This experiment is actually not a direct measurement using photons but is based on the excitation of the analog states of ${}^4\text{He}$ via the ${}^4\text{He}({}^7\text{Li}, {}^7\text{Be})$ reaction. By an ingenious technique to separate spin-nonflip cross sections from spin-flip cross sections, the $\sigma_\gamma(E_\gamma)$ values were deduced, apart from an overall multiplicative factor. The factor was fixed by comparing to the sum of (γ, p) and (γ, n) cross sections at 40 MeV that are taken from the 1983 evaluation [44]. The factor could be slightly larger, however, if it were determined according to the data of Refs. [43, 45] and/or if the $\sigma_\gamma(E_\gamma)$ value at 40 MeV were contributed from a partial cross section (γ, pn) [1]. Then it is probable that the agreement between experiment and theory becomes more perfect.

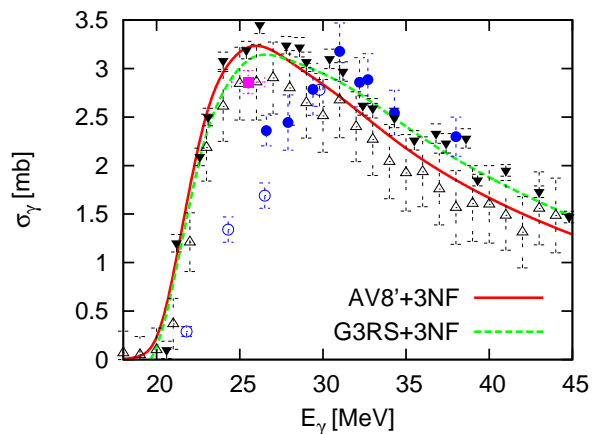


FIG. 9: (Color online) Comparison of the photoabsorption cross section between the CSM calculation with $\theta=17^\circ$ and experiment. The data are taken as follows: closed triangle [43], square [48], open circle [1], closed circle [45], and open triangle [4].

As noted above, serious disagreement between the theory and the experiment [1] is observed at the energy below 30 MeV. Other theoretical calculations [3, 10–12] with the LIT also disagree with the experiment. The experiment makes use of pulsed photons produced via the Compton backscattering of laser photons with high-energy electrons. The cross sections for the two- and three-body decay channels were measured in an event-by-event mode. Since the photons have some intensity distributions with respect to E_γ , the cross section measured is actually a weighted mean of ideal cross sections that are free from the spread of the photon energies and are to be compared to the theoretical cross section. To see the extent to which the energy averaging changes the cross section, we have calculated such cross sections that are weighted by the same distribution functions as used in Refs. [1, 45]. Figure 10 compares the $\sigma_\gamma(E_\gamma)$ values calculated in this way with experiment. The weighting

procedure gives a different effect on the cross section between below and above 30 MeV: Above 30 MeV the original theoretical cross sections change only little and very good agreement with experiment is attained except for the data at 31 MeV. In contrast to this, below 30 MeV the cross sections tend to decrease toward the experimental data points. However, the decrease is not large enough to fill the gap between theory and experiment. The disagreement observed at the low energy region still remains to be accounted for. The experimental method for the generation of incident gamma-rays used in Refs. [1, 45] appears to be very similar to that of Ref. [5], but the method of detecting the particles after the photoabsorption is different. We hope that the discrepancy at the low energy region will be resolved experimentally.

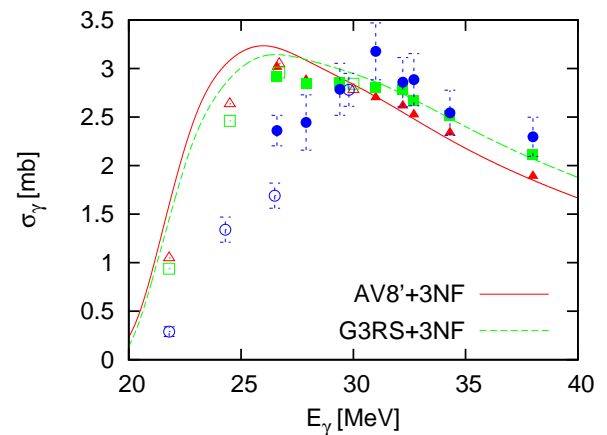


FIG. 10: (Color online) The photoabsorption cross section weighted by the intensity distributions of photons as used in the experiment [1, 45]. Solid and dotted curves are the original theoretical cross sections. Open and closed triangles are the weighted cross sections with AV8'+3NF, while open and closed squares are the results with G3RS+3NF. Open and closed circles are the data taken from Refs. [1, 45].

It is interesting to compare the cross section at high energy. The calculation at high energy region is hard in the MRM but is not difficult in the CSM. A comparison is made in Fig. 11, where E_γ reaches the rest energy of a pion. The G3RS+3NF potential appears to reproduce the data [43] more precisely between 40–80 MeV, but in the other energy region both potentials give equally good results. As mentioned in Sec. IV C, the integrated cross section m_0 for $E_{\text{max}}=135$ MeV is found to agree fairly well with the value estimated using the experimental cross sections. Since the CSM calculation reproduces the total photoabsorption cross section, it is meaningful to analyze the contribution of the two-body decay channels to $\sigma_\gamma(E_\gamma)$. This decomposition can be performed by restricting the sum over the eigenstates λ in Eq. (11) to those whose complex energies lie on the rotating continua starting from the ${}^3\text{H}+p$ and ${}^3\text{He}+n$ thresholds [23, 24, 27]. The cross section labeled as $3N+N$ in the figure denotes this partial cross section. It constitutes

a major part of the total cross section. The cross section labeled Others in the figure is obtained by subtracting the $3N+N$ cross section from the total cross section. As seen in the figure, this quantity is not necessarily positive because of an interference effect. It consists of the three- and four-body decay contributions and more importantly of the interference term of the two-body and other decay amplitudes.

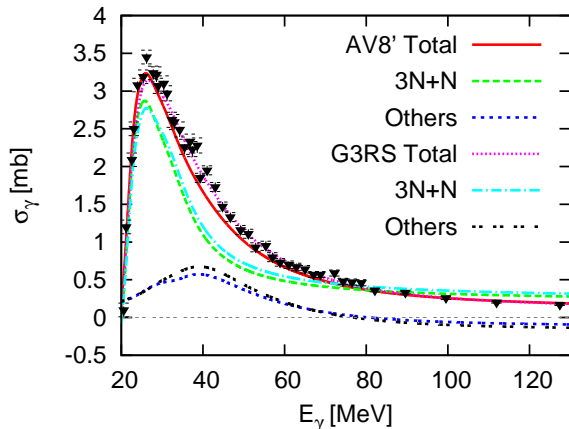


FIG. 11: (Color online) Decomposition of the photoabsorption cross section into the $3N + N$ and other contributions. See the text for how the decomposition is made. The data are taken from Ref. [43].

Another physically interesting decomposition of $\sigma_\gamma(E_\gamma)$ is to make use of the total spin S . As listed in Table I, the ground state of ${}^4\text{He}$ contains by more than 85% the $S=0$ main component and the $S=2$ minor component. The $S=1$ component is negligible. Since the $E1$ operator does not change the spin, it makes sense to decompose the $\sigma_\gamma(E_\gamma)$ value according to the spin channels. Figure 12 displays the decomposition into the partial contributions of $\sigma_\gamma(S=0)$, $\sigma_\gamma(S=2)$, and Others, where Others denotes not only the $S=1$ contribution but also the interfering terms between the different spin amplitudes. This partial cross section, e.g. $\sigma_\gamma(S=0)$, is sensitive to the probability of finding the $S=0$ (and at the same time $L=0$) components in the ground state of ${}^4\text{He}$. If this partial cross section can be measured experimentally, it would give us information on the D -state probability in the ground state of ${}^4\text{He}$, which is closely related to the strength of the tensor force of the NN interaction.

V. CONCLUSIONS

Motivated by the discrepancy in the low-energy data on the photoabsorption cross section of ${}^4\text{He}$, we have performed *ab initio* calculations for the cross section using realistic nuclear forces. Our approach takes proper account of the most important ingredients for a description of four-nucleon dynamics, e.g., correlated motion of the nucleons in both the ground and continuum states of ${}^4\text{He}$,

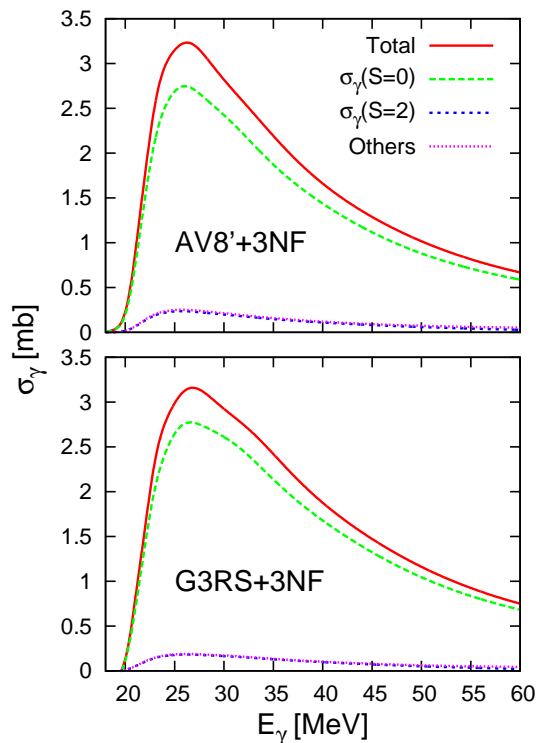


FIG. 12: (Color online) Decomposition of the photoabsorption cross section into contributions specified by the total spin S . See the text for detail.

effects of the tensor force, $3N+N$ -cluster configurations, and final state interactions in the process of the photo-disintegration.

We have applied two different methods, the complex scaling method (CSM) and the microscopic R -matrix method (MRM), to obtain the cross section. The merit of the CSM is that one needs no explicit construction of continuum states but nevertheless gets the photoabsorption cross section in a way similar to bound state problems. The reliability of our approach is confirmed by observing that the two independent methods lead to virtually the same cross section in 20–40 MeV region.

In the energy region between 30–40 MeV the calculated cross sections for ${}^4\text{He}(\gamma, p){}^3\text{H}$ and ${}^4\text{He}(\gamma, n){}^3\text{He}$ are found to agree with the very recent measurements [5, 45]. The total photoabsorption cross section calculated up to the rest energy of a pion is also in fair agreement with most of the available data [4, 43, 45, 48] but the one [1, 45] in the low energy region of 20–30 MeV. The calculated total cross section sharply rises from the ${}^3\text{H}+p$ threshold and reaches a peak at about 26–27 MeV consistently with the Lorentz integral transform calculations, but in disagreement with the data [1, 45]. Hoping to resolve this discrepancy, we have allowed for the energy spread of the photon beams in the measurement and calculated the energy-averaged cross sections using the same distribution functions as those in Ref. [1, 45]. The cross sections in fact decrease below 30 MeV but it turns out

that the change is not large enough to account for the discrepancy.

The configurations that the MRM calculation takes in the internal region are represented by several two-cluster partitions. The ${}^3\text{H}+p$ and ${}^3\text{He}+n$ cluster configurations, among others, are most important to reproduce the photoabsorption cross section in the energy region of 20–35 MeV. This is further corroborated from the analysis of the transition densities as well as the decomposition of the cross section into the $3N+N$ contribution.

The electric dipole transition occurs mainly from the major component with $(L, S)=(0, 0)$ of the ${}^4\text{He}$ ground state to the $(1, 0)$ component of the 1^-1 continuum states. It should be noted, however, that both the ground and 1^-1 excited states gain energy largely from the tensor force, and in fact we have seen an important role of the tensor force induced by the one-pion exchange in enhancing the photoabsorption cross section as well as the photonuclear sum rule.

In this work we have presented the analysis of the electric dipole strength function. A similar analysis for ${}^4\text{He}$ will be possible for other strength functions induced by, e.g., Gamow-Teller and spin-dipole operators that probe different spin-isospin responses of ${}^4\text{He}$. A study along this direction is underway and will be reported elsewhere.

Acknowledgments

We thank T. Shima for many valuable communications and for making some new data available to us prior to publication. Thanks are also due to S. Nakayama and S. Aoyama for useful discussions. W.H. is supported by the Special Postdoctoral Researchers Program of RIKEN. The work of Y.S. is supported in part by a Grant-in-Aid for Scientific Research (No. 21540261) of Japan Society for the Promotion of Science.

-
- [1] T. Shima *et al.*, Phys. Rev. C **72**, 044004 (2005).
 - [2] B. Nilsson *et al.*, Phys. Rev. C **75**, 014007 (2007).
 - [3] S. Quaglioni, W. Leidemann, G. Orlandini, N. Barnea, and V.D. Efros, Phys. Rev. C **69**, 044002 (2004).
 - [4] S. Nakayama *et al.*, Phys. Rev. C **76**, 021305 (2007).
 - [5] W. Tornow, Few-body Syst. **50**, 443 (2011); R.Raut *et al.*, Phys. Rev. Lett. **108**, 042502 (2012).
 - [6] V.G. Efros, W. Leidemann, and G. Orlandini, Phys. Rev. Lett. **78**, 4015 (1997).
 - [7] B. Wachter, T. Mertelmeier, and H.M. Hofmann, Phys. Rev. C **38**, 1139 (1988).
 - [8] D. Gazit, N. Barnea, S. Bacca, W. Leidemann, and G. Orlandini, Phys. Rev. C **74**, 061001 (2006).
 - [9] V.G. Efros, W. Leidemann, G. Orlandini, and A. Barnea, J. Phys. G: Nucl. Part. Phys. **34** R459 (2007) and references therein.
 - [10] D. Gazit, S. Bacca, N. Barnea, W. Leidemann, and G. Orlandini, Phys. Rev. Lett. **96**, 112301 (2006).
 - [11] S. Bacca, Phys. Rev. C **75**, 044001 (2007).
 - [12] S. Quaglioni and P. Navrátil, Phys. Lett. B **652**, 370 (2007).
 - [13] W. Horiuchi and Y. Suzuki, Phys. Rev. C **78**, 034305 (2008).
 - [14] Y. Suzuki, W. Horiuchi, M. Orabi, and K. Arai, Few-Body Syst. **42**, 33 (2008).
 - [15] S.F. Boys, Proc. R. Soc. London Ser. A **258**, 402 (1960).
 - [16] K. Singer, Proc. R. Soc. London Ser. A **258**, 412 (1960).
 - [17] K. Varga and Y. Suzuki, Phys. Rev. C **52**, 2885 (1995).
 - [18] Y. Suzuki and K. Varga, *Stochastic Variational Approach to Quantum-Mechanical Few-Body Problems*, Lecture Notes in Physics, Springer, Berlin (1998), Vol. m54.
 - [19] K. Arai, S. Aoyama, Y. Suzuki, P. Descouvemont, and D. Baye, Phys. Rev. Lett. **107**, 132502 (2011).
 - [20] S. Aoyama, K. Arai, Y. Suzuki, P. Descouvemont, and D. Baye, Few-Body Syst. **52**, 97 (2012).
 - [21] P. Descouvemont and D. Baye, Rep. Prog. Phys. **73**, 036301 (2010).
 - [22] Y.K. Ho, Phys. Rep. **99**, 1 (1983).
 - [23] N. Moiseyev, Phys. Rep. **302**, 211 (1998).
 - [24] S. Aoyama, T. Myo, K. Katō, and K. Ikeda, Prog. Theor. Phys. **116**, 1 (2006).
 - [25] See, for example, P. Ring and P. Schuck, *The Nuclear Many-Body Problem*, Texts and Monographs in Physics, Springer, New York, Heidelberg, Berlin (1980).
 - [26] I. Thompson and F.M. Nunes, *Nuclear Reactions for Astrophysics*, (Cambridge University Press, 2009).
 - [27] T. Myo, K. Katō, S. Aoyama, and K. Ikeda, Phys. Rev. C **63**, 054313 (2001).
 - [28] Y. Suzuki, W. Horiuchi, and D. Baye, Prog. Theor. Phys. **123**, 921 (2010).
 - [29] K. Arai, D. Baye, and P. Descouvemont, Nucl. Phys. A **699**, 963 (2002).
 - [30] K. Arai, S. Aoyama, and Y. Suzuki, Phys. Rev. C **81**, 037301 (2010).
 - [31] B.S. Pudliner, V.R. Pandharipande, J. Carlson, S.C. Pieper, and R.B. Wiringa, Phys. Rev. C **56**, 1720 (1997).
 - [32] R. Tamagaki, Prog. Theor. Phys. **39**, 91 (1968).
 - [33] H. Witała and W. Glöckle, Phys. Rev. C **60**, 024002 (1999).
 - [34] E. Hiyama, B. F. Gibson, and M. Kamimura, Phys. Rev. C **70**, 031001 (2004).
 - [35] H. Kamada *et al.*, Phys. Rev. C **64**, 044001 (2001).
 - [36] E. Hiyama, Y. Kino, and M. Kamimura, Prog. Part. Nucl. Phys. **51**, 223 (2003).
 - [37] P. Mueller *et al.*, Phys. Rev. Lett. **99**, 252501 (2007).
 - [38] D.R. Tilley, H.R. Weller, and G.M. Hale, Nucl. Phys. A **541**, 1 (1992).
 - [39] A. Bohr and B.R. Mottelson, *Nuclear structure*, Vol. II, W.A. Benjamin, Reading (1975).
 - [40] E. Lipparini and S. Stringari, Phys. Rep. **175**, 103 (1989).
 - [41] M. Gari, H. Hebach, B. Sommer, and J.G. Zabolitzky, Phys. Rev. Lett. **41**, 1288 (1978).
 - [42] R. Schiavilla, A. Fabrocini, and V.R. Pandharipande, Nucl. Phys. A **473**, 290 (1987).
 - [43] Yu.M. Arkatov *et al.*, Sov. J. Nucl. Phys. **10**, 639 (1970).
 - [44] J.R. Calarco, B.L. Bermann, and T.W. Donnelly, Phys. Rev. C **27**, 1866 (1983).
 - [45] T. Shima, private communication

- [46] R.E. Florizone *et al.*, Phys. Rev. Lett. **72**, 3476 (1994).
[47] M. Unkelbach and H.M. Hofmann, Nucl. Phys. **A 549**, 550 (1992).
[48] D.P. Wells *et al.*, Phys. Rev. C **46**, 449 (1992).